



## Additive manufacturing of highly reconfigurable plasmonic circuits for terahertz communications

YANG CAO, KATHIRVEL NALLAPPAN,  HICHEM GUERBOUKHA, GUOFU XU,  AND MAKSIM SKOROBOGATIY\*

Department of Engineering Physics, École Polytechnique de Montréal, Montreal, Québec H3T 1J4, Canada

\*Corresponding author: maksim.skorobogatiy@polymtl.ca

Received 26 May 2020; revised 20 July 2020; accepted 20 July 2020 (Doc. ID 398572); published 31 August 2020

While in most existing terahertz communications systems, the THz carrier wave is transmitted via free-space channels, the THz waveguide-based integrated solutions can be of great utility at both the transmitter and receiver ends, thus simplifying the miniaturization and mass production of cost-effective THz communications systems. Here we present a new type of modular THz integrated circuits based on the two-wire plasmonic waveguide components fabricated using a combination of stereolithography (SLA) 3D printing, wet chemistry metal deposition, and hot stamping techniques. Particular attention is paid to the design of the optical circuits based on the two-wire waveguides suspended inside a protective micro-sized enclosure. Such waveguides feature low transmission and bending losses, as well as low dispersion. Using such waveguides as basic building blocks, we then demonstrate several key optical subcomponents, such as low-loss broadband  $2 \times 1$  THz couplers that use two coalescing two-wire waveguide bends, as well as broadband waveguide Bragg gratings that feature a paper sheet with a periodic sequence of metal strips inserted into the air gap of a two-wire waveguide. Finally, using these developed subcomponents, a two-channel add-drop multiplexer is demonstrated to operate at 140 GHz. We believe that the reported micro-encapsulated two-wire waveguide-based modular platform can have a strong impact on the field of THz signal processing and sensing due to the ease of device fabrication and handling, high degree of reconfigurability, and high potential for real-time tunability. © 2020 Optical Society of America under the terms of the OSA Open Access Publishing Agreement

<https://doi.org/10.1364/OPTICA.398572>

### 1. INTRODUCTION

The explosive growth of data traffic over past decades has placed increasing demands on communications systems. With data rates in excess of 100 Gb/s, the terahertz (THz) wireless communications is poised to become an enabling technology for next-generation communications networks [1]. The high directionality and limited propagation range of THz radiation offer enhanced security and resistance to eavesdropping. At the same time, the high directionality of THz radiation poses many challenging engineering problems, such as complexity in discovering the THz network (homing to emitter location) [2], and the necessity for precise alignment between the transmitter and receiver modules, thus requiring the use of advanced beam-steering solutions [3,4]. While mechanical solutions for beam steering issues are available in various forms (such as Galva mirror scanners), a more reliable and robust solution would ideally forgo the use of moving parts and rather employ integrated solutions such as passive and active leaky waveguides and leaky wave antennas [5–9]. In the microwave and THz range, such structures often employ metallic waveguides [10,11] as well as modes propagating along conductive surfaces [12–14], which in THz range are also known as Sommerfeld waves or Zenneck waves depending on the material

of a surface. In this respect, the development of integrated metallic waveguides supporting various types of plasmonic modes is of great interest. Beyond the use in advanced beam steering and detection, integrated THz optical circuits provide a remarkable technological platform for signal processing in THz communications [15,16]. Unlike the cumbersome and prone-to-time-drift assemblies of discrete free-space components, the use of integrated circuits improves long-term reliability, results in a smaller footprint, and is better suited to mass production. Therefore, development of THz integrated optical circuits is a promising direction for signal processing at THz frequencies.

One promising low-loss material that was identified for building THz circuits is silicon. Both total internal reflection waveguides and slab photonic crystal-based waveguides were explored to build THz integrated optical circuits [17]. Various optical elements such as ring resonators, filters, and couplers on silicon substrates have been demonstrated in the THz range [18–23]. However, the fabrication of silicon optical circuits generally requires the use of costly top-of-the-line fab infrastructures such as lithography systems and deep reactive ion etchers, as well as high-cost materials such as gold in a multistage fabrication process. Furthermore, high refractive index contrast normally

associated with silicone photonics results in challenging fabrication tolerances, even for longer THz wavelengths [24]. Finally, silicone integrated photonics is inherently planar, with very limited capacity for 3D integration and out-of-plane interchip connectorization.

Alternatively, the inherently 3D additive manufacturing presents an interesting alternative to the mostly planar silicone photonics. Thus, large-scale THz waveguide-based circuits can be rapidly manufactured with deeply subwavelength precision using readily available low-cost SLA or filament deposition modeling tools. While featuring lower refractive index contrast material combinations than silicone photonics, additive manufacturing results in more relaxed fabrication tolerances and less stringent alignment requirements. Owing to the ubiquitous availability of hardware, the low threshold for entering into production, as well as the ease of 3D integration and out-of-plane interchip interconnect solutions, additive manufacturing emerges as a promising platform for manufacturing waveguide-based optical integrated circuits in the THz spectral range. One of the challenges for additive manufacturing in THz is the lack of low-loss materials to fabricate optical elements with high precision. Particularly, most resins compatible with high-resolution SLA are strong absorbers of the THz light. While some relatively low-loss thermoplastics such as polypropylene [3] are compatible with filament deposition modeling, resolution of such devices is generally not adequate for the fabrication of THz signal processing components that require small fabrication tolerances; for example, an add-drop multiplexer (ADM). In this respect, the search for new materials or novel waveguide designs is of critical importance for 3D-printed THz integrated circuits.

Compared to other reported THz waveguides that were developed for THz communications applications, such as sub-wavelength fibers [3,25], porous fibers [26–28], hollow-core waveguides [29,30], and parallel plate waveguides (PPWG) [31,32], two-wire THz plasmonic waveguides have several advantages that include low transmission loss, negligible group velocity dispersion (GVD), no cut-off frequency, and a high coupling coefficient with conventional linear-polarized THz sources [33]. Most of the two-wire waveguides that were studied earlier featured short sections of straight metallic wires fixed in bulky holders, and were inconvenient to use and unsuitable for building integrated circuits. Although the handling and mechanical stability of the two-wire waveguides can be improved by embedding them into foams or other types of porous dielectric claddings [33–36], the interaction of the modal fields with the lossy materials of the cladding results in increased GVD and transmission losses, thus limiting the utility of classic two-wire waveguides in communications applications.

In this paper, we develop what, to the best of our knowledge, is a novel type of quasi-two-wire waveguides, as well as optical components based on such waveguides using optically thick metal layers deposited onto complex-shaped 3D printed mechanical supports. In fact, the principal goal of this work is to explore THz optical component fabrication using complex metallized 3D shapes that can be readily manufactured using standard SLA 3D printers. The idea is to ultimately go out of plane and pursue 3D optical integration of THz components, which is simply impossible using standard lithographic techniques used in the fabrication of most microwave and optical components. Additionally, for sensing applications as well as for the design of highly tunable THz components we want to have access to the modal fields, which

is especially simple to achieve when using two-wire waveguides [37,38]. Finally, using 3D printing allows seamless integration between the enabling optical elements, such as waveguides and resonators, as well as mechanical support and environmental isolation (that include a protective cage around the waveguide, holders, alignment features and connectors) that ultimately results in convenient to handle, highly modular systems that are easy to assemble and maintain.

Owing to the relatively high resolution ( $\sim 25\ \mu\text{m}$ ), large build volumes ( $\sim 15\ \text{cm} \times 15\ \text{cm}$ ), superior reproducibility, and wide availability, in addition to low infrastructure and maintenance costs, the SLA 3D printing technique is perfectly suited for the fabrication of THz components. As a result, a considerable amount of 3D printing work has been reported for the fabrication of THz dielectric components [39–42]. At the same time, fabrication of THz plasmonic structures is more subtle and less studied due to necessity of the metallization step that must produce high-quality optically thick films (several 100–300 nm for THz frequencies [43]) on complex-shaped polymer surfaces. Recently, efficient metallization and coating techniques for 3D printed parts were reported using standard sputtering techniques [44], as well as more advanced wet or aerosol chemistries with resulting metallic coatings performing comparably to the components machined from bulk metals [45,46].

In this article, we present the in-depth theoretical and experimental studies of the 3D printed two-wire THz plasmonic waveguide-based components and modular optical circuits based on such components. The highly reconfigurable nature of the developed THz plasmonic circuits is demonstrated by assembling nontrivial optical components like an ADM using basic building blocks such as waveguides, bends, Y-splitters, and waveguide Bragg gratings (WBGs), all based on encapsulated two-wire plasmonic waveguides.

This paper is organized as follows. First, we present the fundamental building block of the proposed plasmonic optical circuits: a two-wire waveguide encapsulated into a protective micro-sized cage that can be handled directly and that has various self-alignment features. We start with a numerical study and optimization of the optical guidance properties of such waveguides, including their loss, GVD, and coupling efficiency to the WR6.5 waveguide flange for the operation frequency of  $\sim 140\ \text{GHz}$  set by our experimental setup. Then, the two-wire waveguides are fabricated using SLA 3D printing and wet chemistry deposition techniques, and their performance is experimentally characterized using the continuous wave (CW) THz spectroscopy and a cutback method. Experimentally found waveguide transmission loss and GVD of the straight two-wire waveguide sections (WSs) were measured as  $\sim 6\ \text{m}^{-1}$  and  $-1.5\ \text{ps}/\text{THz}/\text{cm}$  at 140 GHz, respectively. Next, bending losses of the curved two-wire encapsulated waveguides with different bend radiuses and axis of rotation were studied numerically and experimentally. We find that the resin cage significantly reduces bending loss of a two-wire encapsulated waveguide compared to that of a free-standing two-wire waveguide due to modal field enhancement within the cage. We also find that even relatively tight bends with the bending radii of 5 cm result in only a modest increase in the modal propagation loss of less than  $10\ \text{m}^{-1}$ . Next, we explore design and fabrication of paper-based symmetric metal gratings that are made using a low-cost hot stamping technique involving a laser jet printer and metallic thermofoils. Resonant transmission properties of such WBGs can be readily

explained by the destructive interference between the fundamental mode of a two-wire waveguide and the fundamental mode of a planar metallic waveguide formed by the metallic grating elements. Experimentally measured transmission dips with a 25 dB suppression factor and spectral widths as large as 32 GHz (FWHM) at 140 GHz were obtained with 5 cm long, 1.5 mm period WBGs. Finally, we present two reconfigurable THz plasmonic circuits as demonstrators for signal processing in the THz transmitter and receiver circuits, including a THz splitter/multiplexer and an ADM prototype. First, a Y-shaped splitter/multiplexer was fabricated using a combination of two 90° waveguide bends with a 4 cm bend radius; in fact, the splitter is assembled using two 45° waveguide bend sections and a Y-coupler element. Experimentally, we find that the splitter introduces a negligible insertion loss (<0.5 dB) and a very small crosstalk (<−20 dB). Finally, we use a WBG in one of the arms of a Y-splitter and demonstrate a two-channel ADM with In, Through, and Drop ports operating at ~140 GHz and having a spectral width of ~2.8 GHz. We believe that the reported modular

circuits for THz communications, the parameters of a two-wire waveguide are chosen at first to optimize butt-coupling efficiency with a standard WR6.5 waveguide flange (hollow rectangular waveguide with sizes of  $hzWR6 = 825.5 \mu\text{m}$ ,  $hyWR6 = 1651 \mu\text{m}$ ) used for operation at 140 GHz. Figure 1(a) is a schematic of the two waveguides at the coupling plane. To characterize the coupling efficiency between these two waveguides, the mode-matching method is employed that computes the overlap integral between the fundamental mode of the output two-wire waveguide and the excitation mode supported by the input WR6.5 waveguide flange [43,47,48]. Particularly, the vectorial modal electric and magnetic field amplitude distributions of these two butt-coupled waveguides are obtained using the finite element COMSOL Multiphysics. Assuming that all the incoming power is in the fundamental TE<sub>10</sub> mode of the WR6.5 waveguide  $|F_{in}^+\rangle$  with electric field polarized along the shorter side of a waveguide, then ignoring reflections, the complex field coupling coefficient  $C$  into the fundamental mode of the two-wire waveguide  $|F_{out}^+\rangle$  can be found using the following field averages with respect to the longitudinal flux operator  $\hat{S}_z$  as

$$C = \frac{\langle F_{out}^+ | \hat{S}_z | F_{in}^+ \rangle}{\sqrt{\langle F_{out}^+ | \hat{S}_z | F_{out}^+ \rangle \langle F_{in}^+ | \hat{S}_z | F_{in}^+ \rangle}} = \frac{\frac{c}{16\pi} \int dx dy (E_{r,out}^*(x, y) \times H_{r,in}(x, y) + E_{r,in}(x, y) \times H_{r,out}^*(x, y))}{\sqrt{\frac{c}{8\pi} \text{Re} \int dx dy (E_{r,out}^*(x, y) \times H_{r,out}(x, y)) \cdot \frac{c}{8\pi} \text{Re} \int dx dy (E_{r,in}^*(x, y) \times H_{r,in}(x, y))}}, \quad (1)$$

platform based on the micro-encapsulated two-wire waveguides can have a strong impact on the field of integrated optical circuits for THz signal processing and potentially sensing due to the ease of device fabrication, the modular design, and the high degree of reconfigurability, low loss and low dispersion of the underlying waveguides, as well as high potential for the real-time tunability of the optical circuits due to the ease of access of the modal fields inside the controlled in-cage environment.

## 2. TWO-WIRE WAVEGUIDES

### A. Design of the Micro-Encapsulated Two-Wire Waveguide

The main difference between the proposed micro-encapsulated and conventional two-wire waveguides is the presence of a dielectric support. Such support serves several functions, such as shielding of the modal field from the influence of the environment during handling, while also incorporating various alignment features to simplify system integration of several plasmonic components. Particularly, the resin cage with dielectric supports used for wire encapsulation keeps the two wires parallel to each other, while maintaining the gap between the two with high precision due to high definition of the 3D printing process ( $660 \pm 15 \mu\text{m}$  gap over 6 cm long WS). Moreover, several mechanical alignment features are integrated into the cage structure to simplify waveguide coupling to external sources such as horn antennas as well as between different sections of the plasmonic waveguides or other components. With the proper design, the cage surrounding the two wires has only a small effect on the THz surface plasmon polariton (SPP) wave, which is mainly confined to the air region between the two wires.

The THz rectangular metallic waveguides (waveguide flanges) have been widely used in the THz transmitter and receiver circuits. When developing the two-wire waveguide-based plasmonic

where integrals are performed over the whole waveguide cross-sectional plane using transverse modal fields. Note that the modal excitation coefficient (by power) is given by  $|C|^2$ . In simulations, the metallic wires are modeled using the impedance boundary condition (IBC) at the wire surface together with the Drude–Lorentz model for the dielectric constant  $\varepsilon_m$  of silver in THz spectral range taken from [49]

$$\varepsilon_m = 1 - \frac{\omega_p^2}{\omega^2 + i\omega\gamma}, \quad (2)$$

where  $\omega_p = 2\pi \cdot 2.185e15 \text{ Hz}$  is the plasma frequency and  $\gamma_b = 2\pi \cdot 0.5138e13 \text{ Hz}$  is the damping coefficient for the bulk Ag metal.

Figure 1(b) shows the modal electric field distribution of the THz SPP wave supported by the stand-alone two-wire waveguide. The field is mainly confined to the air gap between the two wires, while extending somewhat in the transverse direction from the wires. To optimize the power coupling coefficient between the modes of a WR6.5 waveguide and a two-wire waveguide, we vary the gap size between the wires, as well as the wire diameter. The values of the power coupling coefficient  $|C|^2$  and modal losses (by field) are shown in Figs. 1(e) and 1(f) as blue stars. The maximal power coupling coefficient of 45.43% is obtained using wires featuring the diameter of  $D = 0.4 \cdot hyWR6$  and the gap size of  $AG = 0.8 \cdot hzWR6$ . Then, using the modal field distribution of the fundamental mode of a stand-alone two-wire waveguide, the geometry of the resin cage encapsulating the wires, as shown in Fig. 1(c), was chosen so that the electric field intensity at the internal horizontal and vertical boundaries of the cage do not exceed 3% of the maximal value in the waveguide gap. The plasmonic waveguide losses, as well as the power coupling coefficient between the WR6.5 waveguide flange and micro-encapsulated two-wire waveguides were then recomputed to study the effect of the cage on the waveguide modal properties. The corresponding values of the

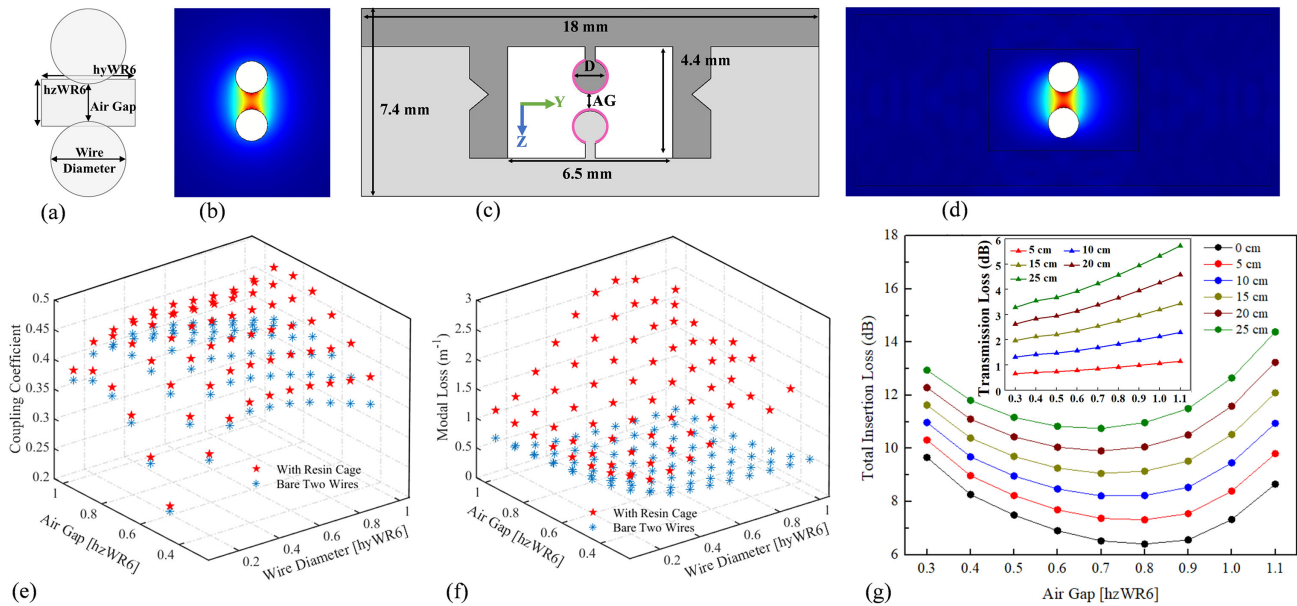


**Fig. 1.** (a) Schematic of the butt-coupling arrangement between a two-wire waveguide and a WR6.5 waveguide flange. (b) Transverse modal electric field amplitude distribution  $|E_z|$  of the THz SPP wave supported by the stand-alone two-wire waveguide at 140 GHz of  $0.8 \cdot \text{hzWR6}$  wire diameter and  $0.8 \cdot \text{hzWR6}$  interwire separation. (c) Schematic of the micro-encapsulated two-wire waveguide cross-section featuring two 3D printed parts (different shades of gray), each featuring a plastic cylinder covered with a silver layer (magenta) that are suspended in air (white) using dielectric supports and encapsulated within a plastic cage (grey). (d) Transverse modal electric field amplitude distribution  $|E_z|$  at 140 GHz for a 3D printed two-wire waveguide with silver layer coated wires placed inside a resin enclosure. The two-wire waveguide geometry is the same as in Fig. 1(b), and the cage size is the same as indicated in Fig. 1(c). (e) Dependence of the power coupling coefficient between the fundamental modes of a WR6.5 waveguide flange and a two-wire waveguide (with and without cage) as a function of the wire diameter and inter-wire separation at 140 GHz. (f) Dependence of the fundamental mode propagation loss (by field) of a two-wire waveguide (with and without cage) as a function of the wire diameter and the interwire separation at 140 GHz. (g) Total insertion losses (in-coupling, out-coupling, and propagation losses by power) of the micro-encapsulated two-wire waveguides featuring different lengths as a function of the interwire separation at 140 GHz. Inset: Propagation losses (by power) of the micro-encapsulated two-wire waveguides of different lengths as a function of the interwire separation at 140 GHz.

coupling coefficient and modal losses are shown in Figs. 1(e) and 1(f) as red stars. In numerical simulations, the refractive index of resin used in 3D printing and its losses are taken from the experimental studies presented in [39]. Particularly, at 140 GHz, their values are  $1.644$  and  $0.225 \text{ cm}^{-1}$  (by field), respectively.

By comparing the transverse electric field distributions of the THz SPP waves supported by the two-wire waveguides with and without the resin cage, as shown in Figs. 1(b) and 1(d), it is noted that presence of a resin cage leads to a somewhat tighter confinement of the fundamental mode in the waveguide gap. This, in turn, leads to a somewhat higher power excitation efficiency of the encapsulated waveguide fundamental mode [47.61% as shown Fig. 1(e)] in the case of an encapsulated waveguide. It also results in the higher propagation losses of such waveguides due to the presence of the modal fields in the lossy material of the cage, as shown in Fig. 1(f). Increased modal confinement due to the presence of the cage can be explained by the “squeezing” of the modal field in the vertical direction ( $Z$ -axis) due to the discontinuity of the electric field component at the top and bottom horizontal boundaries between the cage and the air regions. Particularly, at these boundaries, the  $Z$  component of the electric field dominates. At such boundaries, the  $Z$  displacement field is continuous across the interface; therefore, the dominant  $Z$  component of the electric field in the plastic cage of dielectric constant  $\epsilon_{\text{pl}}$  is going to be smaller than that in the air (with dielectric constant  $\epsilon_{\text{air}}$ ) by the fraction  $\epsilon_{\text{air}}/\epsilon_{\text{pl}}$ , which forces redistribution of the modal field toward the inside of

the cage; hence, the higher presence of the modal field in the gap between the wires.

Moreover, as seen from the red stars in Fig. 1(f), when increasing the wire diameter or the interwire separation (while keeping the cage size the same) the modal size also increases, which leads to an increase in the modal propagation losses due to a stronger overlap with the lossy cage material. It is in contrast to the fundamental mode of a stand-alone two-wire waveguide, whose modal losses decrease when using larger diameter wires or larger interwire separations, as shown by the blue stars in Fig. 1(f) blue stars. It happens due to the lower presence of the modal fields in the lossy metal material of the wires [50].

As seen in Fig. 1(e), the two-wire waveguide excitation efficiency is strongly sensitive to the value of the interwire separation with an optimal value  $AG \approx 0.8 \cdot \text{hzWR6} = 660 \mu\text{m}$ , regardless of the wire diameter. Setting the size of the air gap much smaller or much larger than the optimal value will result in a considerable vector field mismatch between the modes of a two-wire waveguide and a WR6.5 waveguide flange, which is clearly shown in Fig. S2 in Supplement 1, where we show modal intensity distributions for the waveguide flange and the two-wire waveguide featuring different sizes of the air gap. A significant modal mismatch, in turn, will result in a weak coupling between the two waveguides as the excitation efficiency is proportional to the overlap integral between two modes [see Eq. (1)]. At the same time, the excitation efficiency is only weakly sensitive to the wire diameter, as long as it is larger than  $D > 0.4 \cdot \text{hzWR6} = 660 \mu\text{m}$ . From a fabrication point of view,

the interwire distance is defined by the vertical resolution of the printer and is superior to  $25\ \mu\text{m}$  for the SLA printer that we used (Asiga Freeform PRO2). At the same time, the wire shape is rather defined by the transverse resolution of the printer, which is on the order of  $50\text{--}100\ \mu\text{m}$ ; thus, fabrication of the larger wire diameters is more reliable. In our experiments, we found that we can reliably and consistently manufacture waveguides with the optimal interwire separation  $0.8 \cdot \text{hzWR6} = 660\ \mu\text{m}$ , while somewhat larger wire diameters of  $0.8 \cdot \text{hyWR6} = 1.32\ \text{mm}$ . As expected, at  $140\ \text{GHz}$ , the resultant waveguide has relatively high excitation efficiency of  $47.61\%$  (by power) with the WR6.5 flange, which is close to that of the theoretical maximal value of  $48.16\%$ . Moreover, from numerical modeling, we observe that the transverse modal field distributions of the two-wire waveguide and the WR6.5 waveguide flange change little within the operational frequency range of  $110\ \text{GHz}\text{--}170\ \text{GHz}$  (see Fig. S3 in Supplement 1). Therefore, the same high excitation efficiency can be maintained with only a  $\sim 6\%$  variation across all frequencies in this range. Employing the damping coefficient of bulk silver in numerical simulations, theoretical loss (by field) of a straight waveguide is estimated at  $\sim 2.3\ \text{m}^{-1}$ , which is higher than that of a stand-alone two-wire waveguide of  $\sim 0.25\ \text{m}^{-1}$ , while still small enough for the design of practical THz circuits.

For completeness, considering the potential importance of the developed waveguides in applications as interconnects between THz devices in the THz communications systems, the total insertion losses (comprising in-coupling, out-coupling, and propagation losses) of short micro-encapsulated two-wire waveguides featuring different interwire separations are computed by using the

numerically modeled modal losses and excitation efficiency. The corresponding results are summarized in Fig. 1(g). Particularly, we find that the value of the total in/out-coupling loss [black solid line in Fig. 1(g)] is much larger than the propagation loss of the THz light due to material absorption for waveguides shorter than  $\sim 15\ \text{cm}$ . Thus, for shorter micro-encapsulated two-wire waveguides (also the ones used in our work), the minimal total insertion loss is achieved for the interwire separation of  $AG \approx 0.8 \cdot \text{hzWR6}$ . For longer waveguides, however, the lowest total insertion loss is observed for smaller interwire separation, which must be taken into account when designing larger THz circuits.

## B. Fabrication of the Micro-Encapsulated Two-Wire Waveguide

For the convenience of fabrication, the encapsulated two-wire waveguide features two complementary parts, each comprising one wire attached to a half cage using a deeply subwavelength dielectric support ridge with a width of  $150\ \mu\text{m}$  [see Fig. 1(c)]. Although printing along the  $Z$ -axis can greatly reduce the fabrication time, printing large-diameter overhanging wire on a slender support ridge proved to be challenging. Therefore, each part was printed along the waveguide propagation direction ( $X$ -axis) using  $25\ \mu\text{m}$  layer thickness. After polishing the ends of a fully cured structure, the inside of a cage was protected with a masking tape, while leaving only the plastic wire support surface exposed. Next, a silver layer was deposited on top of the plastic using wet chemistry to form conductive surfaces. A two-wire waveguide was finally obtained by assembling the two metallized parts by sliding them into each

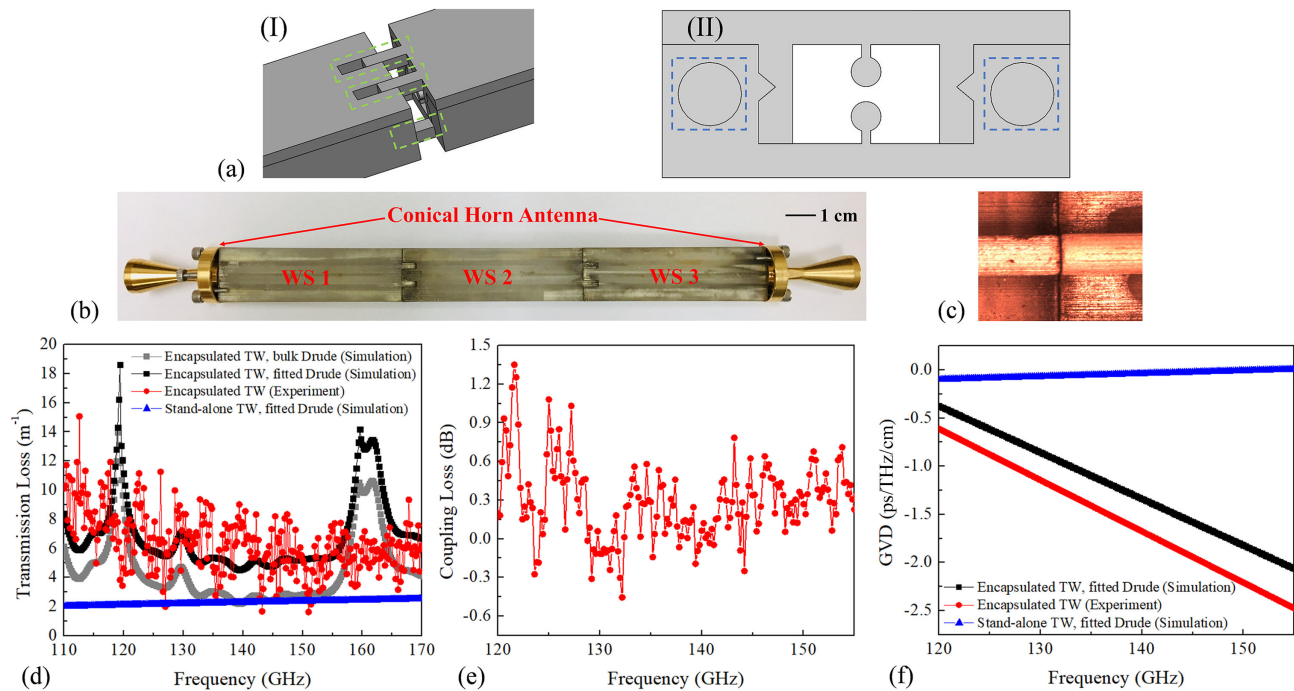


**Fig. 2.** (a) I: Schematic of an interconnect between two plasmonic waveguides. The alignment elements are shown in the green dotted region. II: Schematic of the end face of an encapsulated two-wire waveguide. The screw holes with depths of 5 mm for precision alignment and connectorization with the WR6.5 waveguide flange (of conical horn antenna) are shown in the blue dotted regions. (b) An 18 cm long straight two-wire waveguide assembled by connecting three 6 cm long sections. The two ends of the composite waveguide are fitted with the WR6.5CH-conical horn antennas (Virginia Diodes, Inc.). (c) Enlarged view of the junction between the two wires in a butt-coupling arrangement between the two neighboring WSs. (d) Comparison of the numerical modal losses (by field) for the THz SPP wave and the measured transmission loss (by field) of a straight two-wire waveguide using cutback measurements. (e) Experimentally measured insertion loss (by power) for two butt-coupled waveguides. (f) Numerical simulation and experimental results for the modal GVD for a straight two-wire waveguide.

other using V-grooves and V-ridges that were printed onto the cage to simplify alignment and connectorization [see Fig. 1(c)]. High-quality, 6 cm long WSs were then printed, while longer waveguides were assembled from such sections using another set of alignment and connectorization elements imprinted onto the cage end facets [see Figs. 2(a)-I and 2(b)]. Position and size mismatches between the two wires in the adjacent WSs are mostly due to the precision of the SLA printer and polishing imperfections, which is on the order of several tens of microns [example of a two-wire junction is shown in Fig. 2(c)]. While this issue can bring additional coupling losses, it is expected that they will be small as the mode is mostly guided in the gap between the wires, which is almost 100 times larger in size than the potential misalignment and size mismatch of the wires. Additionally, precise alignment of the encapsulated two-wire waveguide with the WR6.5 waveguide flange (of a conical horn antenna) can be realized by aligning precision screw holes in a flange with judiciously positioned holes in a 3D printed cage [Figs. 2(a)-II and 2(b)].

Additionally, the grain size of the deposited silver layer is on the order of several tens of nanometers [51], while the metal layer is several microns thick. Thus, metal surface roughness would be mostly determined by the roughness of the printed wire-shaped support, which is on the order of several tens of microns. While surface roughness of the metal layer that supports SPP can bring additional scattering loss, such roughness is on a scale much smaller than the wavelength of THz light; thus, it is expected that waveguide losses will be mostly defined by the quality of the nanostructured metallic coating rather than by the imperfections in the shape of a printed wire support.

### 3. OPTICAL CHARACTERIZATION OF THE 3D PRINTED TWO-WIRE WAVEGUIDE COMPONENTS

#### A. Straight Two-Wire Waveguides

The two-wire waveguide transmission losses [see Fig. 2(d)] and coupling losses [see Fig. 2(e)] were deduced from the cutback measurement using composite three-section waveguides similar to the one shown in Fig. 2(b) (see Supplement 1, Section 3.1 for details). The measured transmission loss (by field) is almost constant  $\sim 6 \text{ m}^{-1}$  in the 120–170 GHz frequency range [red curve in Fig. 2(d)], which is almost twice as high as the losses predicted by numerical simulations using the Drude model of bulk silver [grey curve in Fig. 2(d)]. A significant difference between experimentally measured surface plasmon losses in THz and theoretically computed ones using the Drude–Lorentz model of bulk metals is a well-known problem, which is attributed to the surface imperfections and limitations of a Drude model at the metal surfaces [52–55]. In the case of silver layers deposited using wet chemistry (as used in this work), their metal conductivity can be significantly smaller than that of a fine silver sheet because of the nano/micro-crystallization and oxidation effects. While it was demonstrated that for such nanostructured surfaces the Drude–Smith model of metal permittivity could provide more accurate numerical results for THz surface waves, this model is experiment-specific and lacks universality [14,56]. To make the comparison between experimental and numerical work more realistic, and considering that the experimentally characterized operational frequency range of the devices is relatively narrow ( $\sim 110 - 170$  GHz), we retain the simple Drude–Lorentz model of silver for simulations, while

we simply fit the damping factor to achieve the best fit of numerical simulations with the experiment [black and red curves in Fig. 2(d)]. In particular, we find that to reproduce the experimental loss of a straight plasmonic waveguide, the damping factor in the Drude–Lorentz model [Eq. (2)] should be increased by a factor of 50, which is the value  $\gamma_f = 2\pi \cdot 2.69 \times 10^{14} \text{ Hz}$  that is used in all following simulations. We then compare the losses of a stand-alone two-wire waveguide with that of an encapsulated waveguide of identical geometry [blue and black curves in Fig. 2(d)]. We find that stand-alone two-wire waveguides (where ohmic losses dominate) have somewhat smaller, while nevertheless comparable, losses to those of encapsulated waveguides that feature additional loss contribution due to resin cage absorption.

One significant discrepancy between the numerical simulations and loss measurements of micro-encapsulated two-wire plasmonic waveguides is the presence of two strong absorption peaks as predicted theoretically at 119 GHz and 161 GHz with spectral widths of 1.7 GHz and 3.1 GHz (FWDM), respectively. These peaks are due to accidental degeneracy of the dispersion relations of the SPP mode and the high-loss bulk modes of the resin cage. In the vicinity of the degenerate frequency (phase-matching point), the SPP mode hybridizes with the mode of a resin cage, and the resultant dispersion relations of the supermodes exhibit classic avoided crossing behavior. The bandwidth of a loss peak is proportional to the coupling strength between the SPP and the cage mode. The exact shapes of such peaks and their positions are highly sensitive to the scattering losses and structure inhomogeneities (surface roughness) and can easily disappear completely (especially for the narrow peaks) due to the decoherence brought by such imperfections [57]. Therefore, we are not surprised by the absence of such peaks in the measured spectra due to the narrow bandwidth of the peaks, which is most probably caused by the effects of the roughness of the printed structures, as well as cage surface contamination with silver residue during wet chemistry processing. In fact, a more careful implementation of a waveguide with polishing and better controlled wet chemistry deposition of the metal layer allows for observation of avoided crossing resonances, thus making us confident about the good correspondence between the theoretical and experimental results, as well as about our overall understanding of the system (see Supplement 1 for details).

In addition to waveguide losses, one can also extract interwaveguide coupling losses due to a mismatch in the relative size and positions of the neighboring WSs (see Supplement 1, Section 3.1 for details). The coupling loss (by power) data is measured in the 120–155 GHz range [see Fig. 2(e)], with a typical power loss value in the  $\sim 0.4$  dB per connection range, which is significantly smaller than a single WS transmission loss ( $\sim 3$  dB by power for a 6 cm long section). This allows the connection of  $\sim 8$  sections (with a total waveguide length of  $\sim 0.5$  m) before it can start significantly affecting the power budget, thus making us confident that connectorization of many two-wire waveguide-based components is feasible when designing complex THz processing photonic circuits.

Finally, Fig. 2(f) presents experimental data and numerical simulation of the GVD of the SPP mode of a two-wire encapsulated waveguide in the 120–155 GHz spectral range by using

$$\text{GVD} = \frac{\partial^2 \beta(\omega)}{\partial \omega^2} = \frac{\partial^2 (n(\omega) \cdot \omega / c)}{\partial \omega^2}. \quad (3)$$

One reason to pursue development of the plasmonic THz circuits is because of the very small GVDs of the THz SPP waves guided by the classical stand-alone two-wire waveguides [36], which potentially allows processing of extreme data bitrates without scrambling the signal due to temporal pulse dispersion. In the case of encapsulated two-wire waveguides, the GVD of an SPP mode will be higher than that of a stand-alone two-wire waveguide due to the partial overlap of the SPP modal fields with the cage. As shown in Fig. 2(f), the measured GVD of an encapsulated two-wire waveguide is in the 1–2 ps/THz/cm range, which is also in agreement with the results of numerical simulations. While this value is significantly higher than that of a stand-alone two-wire waveguide (less than 0.1 ps/THz/cm), which is shown by the blue curve in Fig. 2(f), it is nevertheless much smaller than the GVD of most alternative THz waveguides, which is normally in the 10 ps/THz/cm range. For all these reasons, we believe that encapsulated two-wire waveguides offer a viable platform for building signal processing THz photonic circuits.

### B. Two-Wire Waveguide Bends

The curved waveguides are of critical importance for building practical photonic circuits and are an integral part of components such as splitters, couplers, ring resonators, and optical delay lines [41,58–60]. Moreover, curved waveguides serve as interconnects between various components in a high-density photonic circuit. Unfortunately, modes guided by curved waveguides are often leaky and prone to higher radiation losses for tighter bends [61]. Additionally, the mode of a bent waveguide has a somewhat different field distribution from that of a straight waveguide; as a result, the coupling between straight and bent waveguides also leads to back reflections and radiative insertion losses, which again are more pronounced for tighter bends. All these negative effects associated with waveguide bends are typically mitigated by increasing the mode confinement, which can be achieved, for example, by

employing high refractive index contrast waveguides (ex. silicon photonics) [62,63]. Importantly, plasmonic modes of a two-wire waveguide show relatively strong confinement in the gap between the two metallic wires, while the effect of bending in such waveguides is less pronounced compared to THz waveguides such as single wires [64], hollow core waveguides [65], and subwavelength fibers [3]. Next, we present numerical and experimental studies of the bending loss of the encapsulated two-wire waveguides and demonstrate that it is significantly smaller than that found in the case of stand-alone two-wire waveguides. We attribute this finding to a stronger confinement of the plasmonic mode in the case of encapsulated wires.

Figures 3(a) and 3(b) show the schematics of the two types of bends that differ from each other by the relative orientation of the bend rotation axis and the two wires. When plotting the modal electric field distributions  $|E|$ , it is noted that their maxima are somewhat shifted from the center of the gap between the two wires and away from the rotational axis, which is a well-known effect of the bend on modal fields, and is also the principal reason for the bend insertion losses. The transmission  $t$  (by field) through a waveguide bend that is connectorized on both sides to straight sections of the same waveguide can be quite generally written as

$$t = |C(R)| \cdot |C(R)| \cdot \exp(-\alpha_{st}l_b) \exp(-\alpha_b(R) \cdot l_b), \quad (4)$$

where  $R$  is the bend radius of the two-wire waveguide bend,  $l_b$  is the length of the waveguide bend,  $\alpha_{st}$  is the transmission loss (by field) of a straight waveguide, and  $\alpha_b(R)$  is an additional loss (by field) due to bending.  $|C(R)|$  is the coupling coefficient (by field) between the bent and straight waveguides, while  $1 - |C(R)|^2$  is the insertion loss (by power) on each side of the bent/straight waveguide connection.

The curved two-wire waveguides were studied using 2D axisymmetric models in COMSOL finite element modeling software that allows the calculation of complex effective refractive

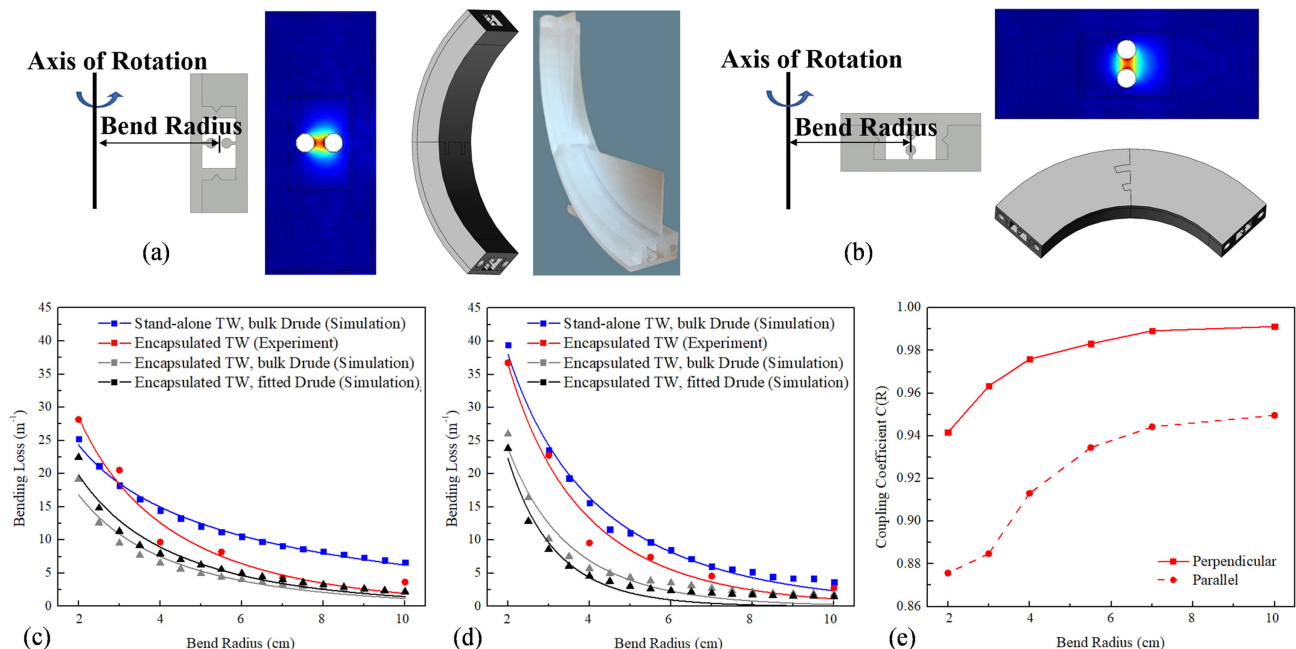


**Fig. 3.** (a) and (b) Schematics and a photo of the two types of the two-wire waveguide 90° bends of 4 cm bend radius and the corresponding modal field distributions  $|E(x, y)|$  of the THz SPP waves at 140 GHz. (c) and (d) Bending losses (by field) of the two types of the waveguide bends. (e) Coupling coefficient  $|C(R)|^2$  (by power) between the encapsulated two-wire waveguide bends and the straight one.

indices of the bend modes. The Ag layer was modeled using IBC with the Drude–Lorentz model in Eq. (2). Figures 3(c) and 3(d) show the results of numerical simulations of bending losses as a function of the bending radius of stand-alone and encapsulated two-wire waveguides as well as their corresponding analytical fit using [66,67]

$$\alpha_b(R) = A \cdot \exp(-B \cdot R) / \sqrt{R}. \quad (5)$$

Compared to the stand-alone two-wire waveguide bends, the encapsulated two-wire waveguide bends show considerably lower bending losses due to enhanced modal confinement brought by the resin cage [blue and gray curves in Figs. 3(c) and 3(d)], as explained in Section 2.A. Moreover, the bending loss is not sensitive to the value of the damping constant [gray and black curves in Figs. 3(c) and 3(d) computed using  $\gamma_b$  and  $\gamma_f$ , respectively]. Finally, Fig. 3(e) shows the power coupling coefficient  $|C(R)|^2$  that was computed using the modal matching approach in Eq. (1) [43], by expanding the mode of a straight encapsulated waveguide into the modes of a bent one (assuming no back reflections).

As a result, bends with the axis of rotation perpendicular to the line connecting the two-wire centers [see Fig. 3(a)] feature somewhat smaller bending losses and a larger coupling coefficient with the straight waveguides than the other bend type [see Fig. 3(b)]. It is due to tighter confinement of the guided mode in the case of the first bend type. Indeed, the effect of the bend is to shift the modal field away from the rotational axis of the bend toward infinity. In the case of a bend in Fig. 3(a), the mode encounters the metal surface of a wire; while in the case of a bend in Fig. 3(b), there is nothing to limit such a shift. Therefore, modes of such a bend show stronger confinement in the core (interwire gap), which also results in lower bending losses.

Next, we experimentally studied losses of the two bend types using 90° bend sections for the bend radii in the range of 2–10 cm at 140 GHz. Due to the limitations of SLA 3D printing, 90° bends were realized by assembling two 45° sections of the same bend radius [see Figs. 3(a) and 3(b)]. The measurements are summarized in Figs. 3(c) and 3(d) (see details in Supplement 1, Section 3.2). While experimental loss is somewhat higher than the theoretical one, the overall tendency is well reproduced. Discrepancies between the experimental and numerical results can be attributed to the effect of printing imperfections such as discrete shape definition by the SLA printer, as well as surface warping during the postprocessing curing step.

### C. Two-Wire Waveguide Bragg Gratings

THz WBGs are of great value for building signal processing components for THz communications. WBGs are often used as band-reject filters, while WBGs with defects are used as band-pass filters. Thus, the integration of even the most simple WBGs into THz photonic circuits can enable such advanced signal processing functionalities as noise filtering or channel adding or dropping when using frequency division multiplexing (FDM). Next, we demonstrate the design and fabrication of strong two-wire WBGs with a stop-band of up to 20 GHz for applications in THz communications within the FDM paradigm. With the operation frequency in the lower THz band of 0.1–0.3 THz, one can pack ~10 of 20 GHz wide channels, each supporting up to 20 GBs data rates. The lower THz band is easily accessible, both with electronics [68,69] and optics-based THz communication systems

[70], with data modulation rates per channel as high as 40 GBs. We therefore believe that the FDM approach in the lower THz band can be a viable approach for multichannel data transmission with total data rates exceeding several 100s GBs.

To fabricate strong WBGs based on the two-wire waveguides, a low-loss dielectric substrate featuring a periodic pattern of metallic stripes is placed into the gap between the two wires. This arrangement results in strong overlap of the waveguide modal fields with the grating region, and as a consequence, wide stop-bands of up to 10% (of the center frequency) can be achieved. While a variety of methods exist for the fabrication of metal patterns on dielectric substrates including laser engraving, lithography, and etching [71–73], such techniques require a relatively expensive infrastructure. In this work, we explored an alternative low-cost and simple hot stamping technique for WBG fabrication. The main advantage of this technique is its similarity to 3D printing because it allows rapid prototyping and extensive fine tuning of the grating geometry with only minimal time and material expenditures. Particularly, 100 μm thick printing paper (Premium Laser Print, Hammermill Inc.,  $n_p = 1.45$ ,  $\alpha_p[\text{cm}^{-1}] = 20.67 \cdot (\omega[\text{THz}])^2 + 1.019$  (by field) [37]) was used as the substrate for the metal grating. The periodic metal pattern was deposited by first printing the required pattern in ink on both sides of the paper symmetrically (Xerox Phaser 6180MFP laser printer), and then transferring the metal/polymer composite from the thermofoil sheet (Deco Foil, Therm O Web) onto the ink-covered paper region. The transfer was achieved by placing the paper in direct contact with thermofoils and heating inside the thermal laminator (Fusion 1100L, Swingline Inc.). The end result is a periodic pattern of a few μm thick aluminum/thermoplastic composite transferred on top of the printed ink pattern [74]. To accommodate the fabricated grating, the enclosure of a 3D printed two-wire waveguide shown in Fig. 1(c) was slightly modified to include two narrow slits in the resin cage throughout the whole length of the waveguide. The grating was then inserted into the slits and self-aligned to be in the center of the air gap between the wires [see Fig. 4(a)].

Operation of the fabricated gratings is easy to understand using the coupled mode theory by considering three principal modes propagating in the two sections of the WBG. Particularly, Fig. 4(b) I shows the schematic of the two sections comprising a single period of the WBG. The first section of width  $w_1$  features a two-wire waveguide with a blank paper sheet in between. The first section transverse cross-section is shown in Fig. 4(b)-II. As the optical thickness of a blank paper (~145 μm) is much smaller than the gap size (~660 μm) and the wavelength of light used in experiments (at 140 GHz  $\lambda \sim 2$  mm), the paper substrate itself does not significantly modify the modal field distribution in the gap between the two wires. Therefore, the effective RI of the fundamental mode propagating in Section 1 (propagation constant of  $\beta_1$ ) is still close to 1 and the modal field distribution resembles that of an empty two-wire waveguide [compare Figs. 4(b)-IV and 1(d)]. At the same time, due to the paper orientation, the modal electric field is mostly perpendicular to the paper surface; thus, the amplitude of the electric field in the paper is reduced compared to that in the air  $|E_p| \approx |E_a|/n_p^2 \sim |E_a|/2$ . The transmission spectrum through a two-wire waveguide with the inserted paper is therefore close to the one without the inserted paper, as shown in Fig. 4(e) (orange curve).

The second section of width  $w_2$  additionally features thin metal plates on both sides of a paper sheet. The second section

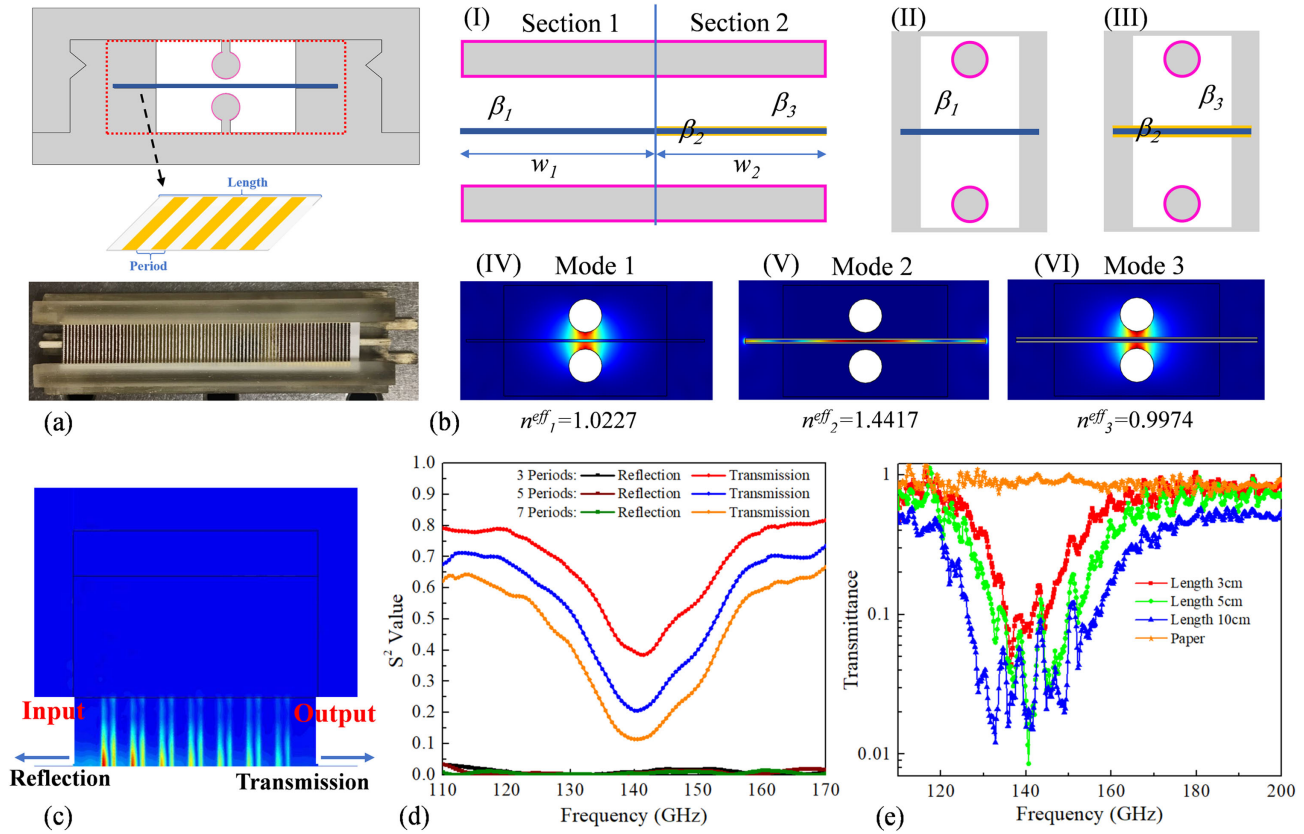


**Fig. 4.** (a) Schematic of the two-wire WBG (top) and a photo from the top with half of the cage removed (bottom). (b) (I) Schematic of a single period of the WBG that comprises two sections, one containing a blank paper sheet, and the other containing metallized paper with the corresponding transverse cross-sections shown in (II) and (III). The electric field distributions ( $|E|$ ) of principal modes propagating in Section 1—Mode 1 (IV), and Section 2—Mode 2 (V), and Mode 3 (VI) at 140 GHz. (c) Simulated modal electric field distribution ( $|E|$ ) of a WBG in the symmetry plane in the mid gap between the two wires at 140 GHz. (d) Simulated power transmission  $|S_{21}|^2$  and reflection  $|S_{11}|^2$  coefficients for WBGs with different number of periods. (e) Experimentally measured transmittance of the paper/metal WBGs of different lengths inserted into a 10 cm-long two-wire waveguide. Transmittance is computed by dividing the grating transmission spectra (by field) by that of an empty two-wire waveguide (reference).

transverse cross-section is shown in Fig. 4(b)-III. In Section 2 of the grating, two kinds of modes are supported. As the paper dielectric substrate is sandwiched by two metal plates, one of the modes [see Fig. 4(b)-V] with propagation constant  $\beta_2$  propagates directly between the metal plates, thus resembling a TEM-like mode of a PPWG. As the corresponding modal field is mainly localized in the paper, the mode 2 effective RI is close to that of the paper 1.45. The other mode propagating in Section 2 (mode 3 with  $\beta_3$ ) is mostly confined to the air region between the metal wires and metal plates. Its modal field distribution and effective RI are similar to those of mode 1 in Section 1 [compare Figs. 4(b)-IV and 4(b)-VI]. At the interface between two sections of a single period, the power coupling coefficient  $\delta$  between highly dissimilar modes 1 and 2 can be computed using the mode-matching method of Eq. (1) [43]. For geometries considered in this paper, we find  $\delta \sim 0.03 - 0.06$ , depending on the configuration. At the same time, the power coupling coefficient between the two similar modes (1 and 3) is high, and assuming small reflection and negligible scattering (radiation) loss at the interface between two sections, it is  $\sim 1 - \delta$ . It then can be shown using the rigorous coupled mode theory that the forward propagating modal fields at the beginning of any period  $|F(x)|$  will be related to the corresponding fields at the beginning of the next period  $|F(x + P)|$  as

$$\begin{aligned}
 |F(x + P)| &\approx |F(x)| \cdot \exp(i\beta_1 w_1) \\
 &\quad \cdot [\delta \cdot \exp(i\beta_2 w_2) + (1 - \delta) \cdot \exp(i\beta_3 w_2)] = \\
 &= |F(x)| \cdot \exp(i\beta_1 w_1 + i\beta_3 w_2) \\
 &\quad \cdot [1 - \delta \cdot (1 - \exp(i(\beta_2 - \beta_3)w_2))].
 \end{aligned} \tag{6}$$

Physically, it means that mode 1 of Section 1 excites two modes (2 and 3) in Section 2, which then propagate with different phase velocities [see Fig. 4(b)]. If modes 2 and 3 recombine destructively at the end of the period, it will result in strong back-reflection, and the grating will be at the stop band. As the phase difference between the two copropagating modes after propagation over one grating period is given by  $(\beta_2 - \beta_3)w_2$ , then, to minimize transmitted power of THz light at the desired Bragg frequency  $\omega_B$ , one has to choose the width  $w_2$  of Section 2 to result in destructive interference between the two modes, so

$$[\beta_2(\omega_B) - \beta_3(\omega_B)]w_2 = \pi \cdot (2m_w + 1), \quad m_w \in \mathbb{N}. \tag{7}$$

Additionally, remembering that modes 1 and 3 are similar [Figs. 4(b)-IV and 4(b)-VI] with very similar propagation constants  $\beta_1 \approx \beta_3$ , and that the grating period is  $P = w_1 + w_2$ , then, for the forward propagating field, we can write

$$|F(x + P)| \approx |F(x)| \cdot \exp(i\beta_1 P) \cdot [1 - 2\delta] = |F(x)| \cdot \exp(i\beta_g P)$$

$$\beta_g = \beta_1 + i \frac{2\delta}{P}, \quad (8)$$

which shows exponential decay of the fields along the grating and also satisfies the block form assuming a complex propagation constant of the WBG. Finally, as propagation along the grating is mostly dominated by modes 1 and 3 with propagation constant  $\beta_1$ , then the reciprocal wavevector of the grating must match the difference between the WBG forward and backward propagating modes, thus resulting in an additional condition for the grating design,

$$2\beta_1 = \frac{2\pi}{P} m_p, \quad m_p \in \mathbb{N}. \quad (9)$$

An example of the numerical study of gratings designed using the resonant design conditions in Eqs. (7) and (9) is presented in [Supplement 1](#), Section 4. The results of transmission and reflection simulations using the COMSOL finite element formulation with ports confirm the validity of our understanding of the grating operation principles. Note that the resonant conditions in Eqs. (7) and (9) result in the most pronounced stop bands and strong reflections, while there are other resonant conditions possible when phase matching the forward propagating mode of a two-wire waveguide with that of the forward or backward propagating modes of a metal plate waveguide. The design complexity and numerous possible resonances in a three-mode grating merit a separate paper, while what follows just aims to present some example of WBGs based on the combination of two-wire and PPWGs.

Next, the two-wire WBGs featuring broad and pronounced transmission dips at 140 GHz are detailed. Such WBGs can serve as efficient band-rejection filters in THz communications circuits. The WBGs are first studied using a 3D modeling frequency domain tool with ports within COMSOL Multiphysics. Because of two reflection symmetry planes, only a quarter of a structure together with a perfect electrical conductor (PEC) and perfect magnetic conductor (PMC) boundary conditions can be used. The metalized patterns on paper are defined using the IBC boundary condition with the Drude–Lorentz model for bulk aluminum ( $\omega_{Al} = 2\pi \cdot 3.57e15$  Hz,  $\gamma_{Al} = 2\pi \cdot 1.94e13$ ). In simulations, the THz light is launched using the port boundary condition at the input facet of the WBGs containing seven periods. By monitoring the power transmission coefficient at the other facet of the WBGs ( $|S_{21}|^2$ ), it is noted that gratings with a period of 1.5 mm and a metalized-paper section width  $w_2$  of 0.7 mm feature pronounced transmission dips at 140 GHz [see Figs. 4(d) and 4(e)]. At the same time, the power reflection coefficient ( $|S_{11}|^2$ ) in such a design is small (less than 3%). A more detailed analysis shows that in this type of grating the forward propagating mode of a metal plate waveguide is matched to the backward propagating mode of a metal plate waveguide, which has only a small coupling with the backward propagating mode of two-wire waveguides. In other words, such a grating, while featuring a large stop-band, is also characterized by low reflection into the two-wire waveguide that feeds it.

In the experiments, we used gratings of different lengths that featured periodic sequences with 19, 32, and 65 metal strips on paper substrates placed into the gap of 10 cm two-wire waveguide. It was then characterized in a setup detailed in [Supplement 1](#),

Section 3.1. The grating transmittance was obtained by comparing the transmission spectra (by field) of the two-wire waveguide with and without the gratings [see Fig. 4(e)]. A pronounced transmission dip at 140 GHz featuring a spectral width of 32 GHz (FWDM) and a minimum relative transmittance below  $10^{-2}$  is obtained using the grating with a length of 5 cm. Additionally, when increasing the grating length to 10 cm, the transmission dip becomes even more pronounced.

In passing, we note the presence of ripples in the measured transmission spectra (see, for example, Figs. 2, 4, 5, and 6). The origin of these ripples is a standing-wave phenomenon, which is particular to the coherent CW THz spectroscopy setup used in our experiments. In fact, there are two types of ripples. The most pronounced ones are caused by the multiple reflections inside of the two silicon lenses (size  $d \sim 10$  mm,  $n_{Si} \sim 3.42$ ) that are integrated into the THz photomixers in the emission and detection arms. The corresponding frequency separation between the two ripples of this kind is given by  $\Delta\nu_1 = c/2dn_{Si} \sim 4$  GHz. The second type of ripple is due to standing waves formed between the reflections on the free-space optical components (ex. parabolic mirrors and plano-convex lenses). These ripples have smaller amplitudes and are more closely spaced in the frequency domain. Although the effect of the first type of ripple can be somewhat mitigated by normalizing the measured spectra with respect to [57], the effect of the second type of ripple is more difficult to alleviate as the free-space path within the setup normally changes during measurements.

## 4. THz PLASMONIC CIRCUITS

In this section, we demonstrate the possibility of building highly reconfigurable plasmonic circuits using examples of a THz splitter/multiplexer and a two-channel ADM.

### A. THz Splitter/Multiplexer

A Y-shaped THz splitter/multiplexer was fabricated by fusing two  $90^\circ$  two-wire waveguide bends with a 4 cm bending radius (axis of rotation parallel to the line connecting the wire centers), as shown in Fig. 5(a). Furthermore, the two curved sections are terminated with short 0.5 cm sections of a straight waveguide for ease of connectorization with other components. Such a coupler can be used either as a broadband 50/50 splitter or a multiplexer of two data streams.

In the first experiment, we test a Y-coupler operation in the splitter mode. The THz light is launched into port 1 via a WR6.5 conical horn antenna, then divided in the Y-shaped splitter, and finally registered at ports 2 and 3, each featuring a WR6.5 conical horn antenna. Figure 5(b) shows the transmittances of the output ports, which are obtained by dividing the transmission spectra (by field) of light coming from ports 2 and 3 by that of the THz light launched into port 1 (for more details, see [Supplement 1](#), Section 5). The data shows that the transmittances of the two output ports are very similar, with only few percentage difference in the 100–200 GHz operation frequency range.

In the second experiment, we test a Y-coupler operation in the multiplexer mode. The THz light is launched into port 3 (or port 2), then travels through the Y-junction, and finally leaves the component through port 1 and partially through unused port 2 (or port 3, correspondently). For example, Fig. 5(c) shows the transmittances of the ports 1 and 3, which are obtained by dividing the transmission spectra (by field) measured at these ports by the

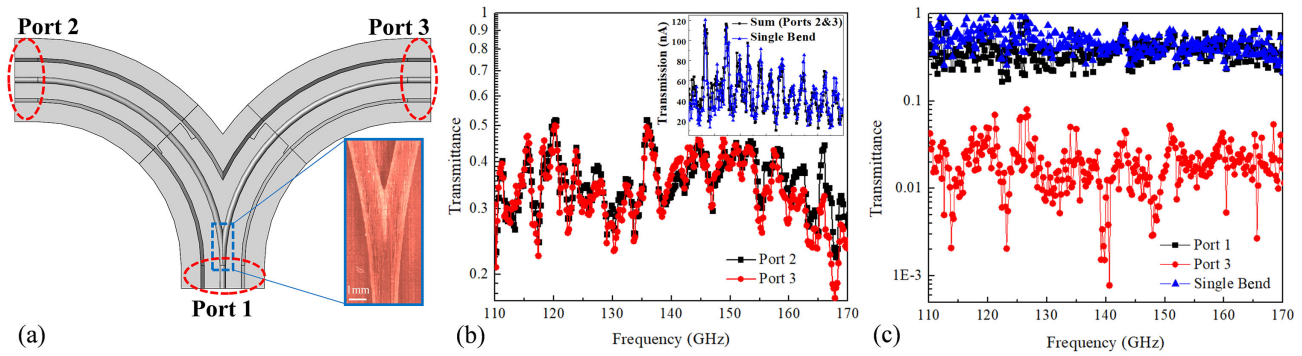


**Fig. 5.** (a) Schematic (half) of a Y-shaped splitter/multiplexer that uses two fused two-wire waveguide bends. In red dotted regions are the 0.5-cm section of straight waveguides. Inset: Photo of the two fused wires in a blue dotted region of a schematic. (b) Transmittance of the output ports 2 and 3 with the incident THz light in port 1. It is computed by dividing the transmission spectra (by field) of the THz light received at the corresponding output ports of a splitter by the one launched into port 1. Inset: Comparison of the two transmission spectra (by field), one (black) is obtained by summing the outputs of the ports 2 and 3 when light is launched into port 1, while the other (blue) is obtained by measuring a single bend section with the equivalent geometry of a half splitter [shown in Fig. 3(b)], thus signifying a minimal scattering loss at a Y-junction. (c) Transmittance of the output ports 1 (black) and 3 (red) when the THz light is launched into port 2, compared to the scattering of a single bend section of the equivalent geometry (blue) shown in Fig. 3(b). Transmittance is computed by dividing the transmission spectra (by field) of the THz light recorded at the output ports of a multiplexer by that of the incident THz light.

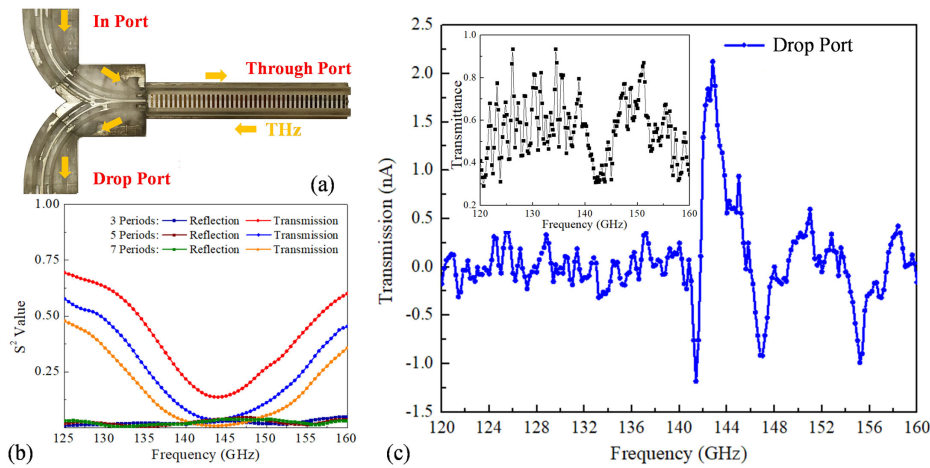


**Fig. 6.** (a) Two-wire waveguide-based ADM composed of a Y-coupler and a WBG. (b) Numerical results of the transmission ( $|S_{21}|^2$ ) and reflection ( $|S_{11}|^2$ ) of WBGs with a period of 2.3 mm and a duty cycle of 55%. (c) Recorded spectrum (field amplitude) of the ADM measured at the Drop port. Inset: Transmittance (by field) of the stand-alone WBG integrated into the ADM.

spectrum of the THz light launched into port 2. Note that parasitic transmission through port 3 (due to back-scattering at the Y-junction) is much weaker (on average, by  $-50$  dB by power) than the intended forward signal transmission through port 1, which signifies that the developed component can be used as a  $2 \times 1$  multiplexer.

Furthermore, by comparing the net (sum) intensity of THz light measured at the output ports 1 (and 2) of the Y-coupler to the light intensity transmitted through a single bend of identical geometry [see blue curves in Figs. 5(b) inset and Fig. 5(c)], we conclude that the average insertion loss brought by the Y-junction is small  $\sim 0.3$  dB at  $\sim 140$  GHz.

### B. THz ADM

The ADM is a key building block in all communications systems that use FDM. Many ADM designs in the near-infrared telecommunications band use fiber Bragg gratings and circulators [75], a concept that is translated in our current work into THz range.

Alternatively, THz ADMs also were build using photonic band gap materials and ring resonators [76,77]. Such devices, however, were obtained using complex and costly microfabrication processes in which high-resistivity float zone silicon wafer was machined to obtain the periodically arranged posts, and then the array was sandwiched by two metal plates using eutectic bonding.

In this section, as a proof of concept, we demonstrate a simple ADM with a  $\sim 2.8$  GHz bandwidth (FWHM) that operates at  $\sim 140$  GHz by integrating a Y-coupler and a WBG based on the two-wire waveguide technology discussed earlier. The ADM is shown in Fig. 6(a). A signal featuring several mixed stand-alone channels at different frequencies (FDM modality) is launched into the In port. After propagation through a curved waveguide of a Y-coupler, the signal arrives to a WBG where the channel in the grating stopband is back reflected, while the rest of the channels continue into the Through port. In the absence of a THz circulator, the reflected channel is then split 50/50 by the Y-coupler and it finally arrives to the Drop port. Note that THz circulators have

been demonstrated earlier (ex. [78]) and they are fully compatible with the two-wire waveguide base technology used in this work.

At first, we study the WBGs used in the ADM prototype with COMSOL Multiphysics. By analyzing the transmission and reflection spectra of gratings featuring different pitches, we find that transmission dips and reflection peaks can be obtained at  $\sim 140$  GHz using gratings with a period of 2.3 mm and a duty cycle of 55% ( $w_2 = 1.27$  mm) [see Fig. 6(b)]. Here we present a simulation using lossy versus lossless paper substrate material. Compared to the grating of 1.5 mm period discussed earlier [see Fig. 4(d)], gratings used in the ADM prototype feature somewhat narrower stop bands, while at the same time they feature significant reflected power in the stop band ( $|S_{11}|^2 \sim 30\%$  lossless paper, and  $|S_{11}|^2 \sim 6\%$  lossy paper), which makes them suitable to build ADMs. Note that paper loss has significant negative effect on the reflected power and, in the future work, alternative substrates will be used in gratings. Experimentally, a 6.9 mm-wide paper sheet featuring 43 grating periods of 2.3 mm pitch and symmetric arrangement of metal stripes on both sides of the paper substrate was prepared as described in Section 3. A resultant 10 cm long WBG was measured and showed a minimal relative transmittance (by field) of 0.3 with a  $\sim 4$  GHz (FWHM) transmission dip at the Bragg frequency of 142.6 GHz [see Fig. 6(c) Inset]. Finally, Fig. 6(c) shows the measured spectra at the Drop port of the ADM that uses the abovementioned WBG in the Through arm of the device (for details of the measurement, see Supplement 1, Section 6). The dropped target range of  $\sim 141 - 145$  GHz is clearly visible at the Drop port of the ADM despite the low reflection efficiency of the grating.

Finally, the simulations suggest that considerably more efficient (in reflection) gratings can be designed using classic a quarter-wave condition for each section in the period, or even using more relaxed design criteria, as shown in Eqs. (7) and (9); however, such gratings cannot be reliably manufactured using the simple hot stamping technique that was explored in this paper because they require significantly smaller metallic features and lower-loss substrates. We therefore consider the results of this section as a proof of principle with a clear path for optimization to be pursued in future works.

## 5. CONCLUSION

In this work, 3D printed micro-encapsulated two-wire THz plasmonic waveguide components and circuits have been investigated theoretically and experimentally. Modular THz components and reconfigurable circuits are built based on two-wire waveguides featuring two metallized plastic wire substrates suspended in air on deeply subwavelength supports and encapsulated inside a protective resin cage. Such components are fabricated using highly precise, efficient, and low-cost SLA 3D printing enhanced with a wet chemistry metal deposition technique. Using CW-THz spectroscopy, we first characterized the transmission loss and the GVD of straight waveguides at 140 GHz, which are  $\sim 6$  m $^{-1}$  (by field) and  $-1.5$  ps/THz/cm, respectively. Next, the bending loss of bent two-wire waveguides was characterized experimentally as a function of bending radii for two different types of bend geometry. It was concluded that the presence of the encapsulating cage significantly reduces the bending loss due to a stronger confinement of light in the gap between the two wires compared to the case of stand-alone two-wire waveguides. We find that even for a small bending radius of  $\sim 5$  cm, the experimental bending loss does not exceed  $\sim 10$  m $^{-1}$  (by field). Next, we detailed two-wire WBGs

that feature a thin paper sheet with a periodic sequence of metal strips placed in the gap between two wires. Metallized gratings were fabricated using a rapid prototyping hot stamping technique using thermofoils, laser-printed templates, and a laminator. Experimentally, we find that even short 5 cm long WBGs of this design can exhibit transmission dips with a minimal relative transmittance below  $10^{-2}$  and a spectral width of 32 GHz. Finally, two kinds of THz plasmonic circuit prototypes were demonstrated, including a Y-shaped THz splitter/multiplexer that employs two coalescing waveguide bends, as well as an ADM that employs a reflective WBG. Experimentally, we find that the Y-shaped coupler features a negligible insertion loss ( $< 0.5$  dB) and transmission loss almost identical to that of a stand-alone bend section employed in its design. Finally, we found experimentally that an ADM exhibits a designed drop functionality with a spectral bandwidth of 2.8 GHz at the Bragg frequency of  $\sim 140$  GHz. Based on these findings we therefore conclude that the proposed 3D printed THz two-wire waveguides and components based on such waveguides present a viable technology for robust, cost-effective, and highly reconfigurable THz optical circuits for signal processing and sensing applications.

**Funding.** Canada Research Chairs (34633); China Scholarship Council (201706250016).

**Disclosures.** The authors declare that there are no conflicts of interest related to this paper.

See Supplement 1 for supporting content.

## REFERENCES

1. T. Kleine-Ostmann and T. Nagatsuma, "A review on terahertz communications research," *J. Infrared Millim. Terahertz Waves* **32**, 143–171 (2011).
2. Y. Ghasempour, R. Shrestha, A. Charous, E. Knightly, and D. M. Mittleman, "Single-shot link discovery for terahertz wireless networks," *Nat. Commun* **11**, 2017 (2020).
3. K. Nallappan, Y. Cao, H. Guerboukha, C. Nerguizian, and M. Skorobogaty, "Dispersion limited versus power limited terahertz transmission links using solid core subwavelength dielectric fibers," *enrXiv* 10.31224/osf.io/bjpdm (2020).
4. Z. Chen, X. Ma, B. Zhang, Y. Zhang, Z. Niu, N. Kuang, W. Chen, L. Li, and S. Li, "A survey on terahertz communications," *China. Commun.* **16**, 1–35 (2019).
5. S. Taravati and C. Caloz, "Mixer-duplexer-antenna leaky-wave system based on periodic space-time modulation," *IEEE Trans. Antennas Propag.* **65**, 442–452 (2016).
6. A. Al-Bassam, S. Otto, D. Heberling, and C. Caloz, "Broadside dual-channel orthogonal-polarization radiation using a double-asymmetric periodic leaky-wave antenna," *IEEE Trans. Antennas Propag.* **65**, 2855–2864 (2017).
7. L. Liu, C. Caloz, and T. Itoh, "Dominant mode leaky-wave antenna with backfire-to-endfire scanning capability," *Electron. Lett.* **38**, 1414–1416 (2002).
8. C. Caloz, T. Itoh, and A. Rennings, "CRLH metamaterial leaky-wave and resonant antennas," *IEEE Antennas Propag. Mag.* **50**(5), 25–39 (2008).
9. N. J. Karl, R. W. McKinney, Y. Monnai, R. Mendis, and D. M. Mittleman, "Frequency-division multiplexing in the terahertz range using a leaky-wave antenna," *Nat. Photonics* **9**, 717–720 (2015).
10. B. Bowden, J. A. Harrington, and O. Mitrofanov, "Low-loss modes in hollow metallic terahertz waveguides with dielectric coatings," *Appl. Phys. Lett.* **93**, 181104 (2008).
11. J. A. Harrington, R. George, P. Pedersen, and E. Mueller, "Hollow polycarbonate waveguides with inner Cu coatings for delivery of terahertz radiation," *Opt. Express* **12**, 5263–5268 (2004).

12. T. I. Jeon, J. Zhang, and D. Grischkowsky, "THz Sommerfeld wave propagation on a single metal wire," *Appl. Phys. Lett.* **86**, 161904 (2005).
13. C. R. Williams, S. R. Andrews, S. A. Maier, A. I. Fernández-Domínguez, L. Martín-Moreno, and F. J. García-Vidal, "Highly confined guiding of terahertz surface plasmon polaritons on structured metal surfaces," *Nat. Photonics* **2**, 175–179 (2008).
14. M. Poulin, S. Giannacopoulos, and M. Skorobogatiy, "Surface wave enhanced sensing in the terahertz spectral range: modalities, materials, and perspectives," *Sensors* **19**, 5505 (2019).
15. B. Vidal, T. Nagatsuma, N. J. Gomes, and T. E. Darcie, "Photonic technologies for millimeter- and submillimeter-wave signals," *Adv. Opt. Technol.* **2012**, 925065 (2012).
16. W. Withayachumnankul, M. Fujita, and T. Nagatsuma, "Integrated silicon photonic crystals toward terahertz communications," *Adv. Opt. Mater.* **6**, 1800401 (2018).
17. K. Tsuruda, M. Fujita, and T. Nagatsuma, "Extremely low-loss terahertz waveguide based on silicon photonic-crystal slab," *Opt. Express* **23**, 31977–31990 (2015).
18. J. Li, J. He, and Z. Hong, "Terahertz wave switch based on silicon photonic crystals," *Appl. Opt.* **46**, 5034–5037 (2007).
19. M. Yata, M. Fujita, and T. Nagatsuma, "Photonic-crystal diplexers for terahertz-wave applications," *Opt. Express* **24**, 7835–7849 (2016).
20. S. Li, H. Liu, Q. Sun, and N. Huang, "A tunable terahertz photonic crystal narrow-band filter," *IEEE Photon. Technol. Lett.* **27**, 752–754 (2015).
21. H. W. Hübers, "Terahertz technology: Towards THz integrated photonics," *Nat. Photonics* **4**, 503–504 (2010).
22. X. Yu, R. Yamada, J. Y. Kim, M. Fujita, and T. Nagatsuma, "Integrated circuits using photonic-crystal slab waveguides and resonant tunneling diodes for terahertz communication," in *Progress in Electromagnetics Research Symposium (PIERS)*, (IEEE, 2018), pp. 599–605.
23. F. Fan, Y. Hou, Z. W. Jiang, X. H. Wang, and S. J. Chang, "Terahertz modulator based on insulator-metal transition in photonic crystal waveguide," *Appl. Opt.* **51**, 4589–4596 (2012).
24. J. Dai, J. Zhang, W. Zhang, and D. Grischkowsky, "Terahertz time-domain spectroscopy characterization of the far-infrared absorption and index of refraction of high-resistivity, float-zone silicon," *J. Opt. Soc. Am. B* **21**, 1379–1386 (2004).
25. M. Roze, B. Ung, A. Mazhorova, M. Walther, and M. Skorobogatiy, "Suspended core subwavelength fibers: towards practical designs for low-loss terahertz guidance," *Opt. Express* **19**, 9127–9138 (2011).
26. A. Hassani, A. Dupuis, and M. Skorobogatiy, "Low loss porous terahertz fibers containing multiple subwavelength holes," *Appl. Phys. Lett.* **92**, 071101 (2008).
27. A. Hassani, A. Dupuis, and M. Skorobogatiy, "Porous polymer fibers for low-loss terahertz guiding," *Opt. Express* **16**, 6340–6351 (2008).
28. K. Nallappan, H. Guerboukha, Y. Cao, C. Nerguizian, and M. Skorobogatiy, "Experimental demonstration of 5 Gbps data transmission using long subwavelength fiber at 140 GHz," in *IEEE Radio and Wireless Symposium (RWS)* (IEEE, 2019), pp. 1–4.
29. H. Bao, K. Nielsen, O. Bang, and P. U. Jepsen, "Dielectric tube waveguides with absorptive cladding for broadband, low-dispersion and low loss THz guiding," *Sci. Rep.* **5**, 7620 (2015).
30. A. Dupuis, K. Stoeffler, B. Ung, C. Dubois, and M. Skorobogatiy, "Transmission measurements of hollow-core THz Bragg fibers," *J. Opt. Soc. Am. B* **28**, 896–907 (2011).
31. R. Mendis and D. Grischkowsky, "Undistorted guided-wave propagation of subpicosecond terahertz pulses," *Opt. Lett.* **26**, 846–848 (2001).
32. R. Mendis and D. M. Mittleman, "Comparison of the lowest-order transverse-electric (TE<sub>1</sub>) and transverse-magnetic (TEM) modes of the parallel-plate waveguide for terahertz pulse applications," *Opt. Express* **17**, 14839–14850 (2009).
33. M. Mbyone, R. Mendis, and D. Mittleman, "A terahertz two-wire waveguide with low bending loss," *Appl. Phys. Lett.* **95**, 233506 (2009).
34. A. Markov, H. Guerboukha, and M. Skorobogatiy, "Hybrid metal wire-dielectric terahertz waveguides: challenges and opportunities," *J. Opt. Soc. Am. B* **31**, 2587–2600 (2014).
35. J. Anthony, R. Leonhardt, and A. Argyros, "Hybrid hollow core fibers with embedded wires as THz waveguides," *Opt. Express* **21**, 2903–2912 (2013).
36. A. Markov and M. Skorobogatiy, "Two-wire terahertz fibers with porous dielectric support," *Opt. Express* **21**, 12729–12743 (2013).
37. G. Yan, A. Markov, Y. Chinifooroshan, S. M. Tripathi, W. J. Bock, and M. Skorobogatiy, "Low-loss terahertz waveguide Bragg grating using a two-wire waveguide and a paper grating," *Opt. Lett.* **38**, 3089–3092 (2013).
38. G. Yan, A. Markov, Y. Chinifooroshan, S. M. Tripathi, W. J. Bock, and M. Skorobogatiy, "Resonant THz sensor for paper quality monitoring using THz fiber Bragg gratings," *Opt. Lett.* **38**, 2200–2202 (2013).
39. J. Li, K. Nallappan, H. Guerboukha, and M. Skorobogatiy, "3D printed hollow core terahertz Bragg waveguides with defect layers for surface sensing applications," *Opt. Express* **25**, 4126–4144 (2017).
40. A. D. Squires, E. Constable, and R. A. Lewis, "3D printed terahertz diffraction gratings and lenses," *J. Infrared Millim. Terahertz Waves* **36**, 72–80 (2015).
41. M. Weidenbach, D. Jahn, A. Rehn, S. F. Busch, F. B. Mejía, J. C. Balzer, and M. Koch, "3D printed dielectric rectangular waveguides, splitters and couplers for 120 GHz," *Opt. Express* **24**, 28968–28976 (2016).
42. T. Ma, H. Guerboukha, M. Girard, A. D. Squires, R. A. Lewis, and M. Skorobogatiy, "3D printed hollow-core terahertz optical waveguides with hyperuniform disordered dielectric reflectors," *Adv. Opt. Mater.* **4**, 2085–2094 (2016).
43. M. Skorobogatiy, *Nanostructured and Subwavelength Waveguides: Fundamentals and Applications* (JWS, 2012).
44. S. Pandey, B. Gupta, and A. Nahata, "Terahertz plasmonic waveguides created via 3D printing," *Opt. Express* **21**, 24422–24430 (2013).
45. T. Ma, K. Nallapan, H. Guerboukha, and M. Skorobogatiy, "Analog signal processing in the terahertz communication links using waveguide Bragg gratings: example of dispersion compensation," *Opt. Express* **25**, 11009–11026 (2017).
46. D. A. Kovacevich, L. Lei, D. Han, C. Kuznetsova, S. E. Kooi, H. Lee, and J. P. Singer, "Self-limiting electrospray deposition for the surface modification of additively-manufactured parts," *ACS Appl. Mater. Interfaces* **12**, 20901–20911 (2020).
47. H. Pahlevaninezhad, T. E. Darcie, and B. Heshmat, "Two-wire waveguide for terahertz," *Opt. Express* **18**, 7415–7420 (2010).
48. H. Pahlevaninezhad and T. E. Darcie, "Coupling of terahertz waves to a two-wire waveguide," *Opt. Express* **18**, 22614–22624 (2010).
49. X. Zhang, Y. L. Chen, R. S. Liu, and D. P. Tsai, "Plasmonic photocatalysis," *Rep. Prog. Phys.* **76**, 046401 (2013).
50. K. L. Wang and D. M. Mittleman, "Metal wires for terahertz wave guiding," *Nature* **432**, 376–379 (2004).
51. T. Wen, J. Gao, B. Bian, and J. Shen, "Investigation on roughness of silver thin films inside silica capillaries for hollow waveguides," *Mater. Lett.* **50**, 124–128 (2001).
52. J. S. Jo, T. I. Jeon, and D. Grischkowsky, "Prototype 250 GHz bandwidth chip to chip electrical interconnect, characterized with ultrafast optoelectronics," *IEEE Trans. Terahertz Sci. Technol.* **3**, 453–460 (2013).
53. N. Laman and D. Grischkowsky, "Reduced conductivity in the terahertz skin-depth layer of metals," *Appl. Phys. Lett.* **90**, 122115 (2007).
54. M. Nazarov and J. L. Coutaz, "Terahertz surface waves propagating on metals with sub-wavelength structure and grating reliefs," *J. Infrared Millim. Terahertz Waves* **32**, 1054–1073 (2011).
55. A. J. Shutter and D. Grischkowsky, "Gap independent coupling into parallel plate THz waveguides using cylindrical horn antennas," *J. Appl. Phys.* **112**, 073102 (2012).
56. T. L. Cocker, D. Baillie, M. Buruma, L. V. Titova, R. D. Sydora, F. Marsiglio, and F. A. Hegmann, "Microscopic origin of the Drude-Smith model," *Phys. Rev. B* **96**, 205439 (2017).
57. Y. Cao, K. Nallappan, H. Guerboukha, T. Gervais, and M. Skorobogatiy, "Additive manufacturing of resonant fluidic sensors based on photonic bandgap waveguides for terahertz applications," *Opt. Express* **27**, 27663–27681 (2019).
58. J. Ma, M. Weidenbach, R. Guo, M. Koch, and D. M. Mittleman, "Communications with THz waves: switching data between two waveguides," *J. Infrared Millim. Terahertz Waves* **38**, 1316–1320 (2017).
59. K. S. Reichel, R. Mendis, and D. M. Mittleman, "A broadband terahertz waveguide T-junction variable power splitter," *Sci. Rep.* **6**, 28925 (2016).
60. B. Wang and P. W. Guo, "Plasmonic waveguide ring resonator at terahertz frequencies," *Appl. Phys. Lett.* **89**, 133106 (2006).
61. J. Saijonmaa and D. Yevick, "Beam-propagation analysis of loss in bent optical waveguides and fibers," *J. Opt. Soc. Am.* **73**, 1785–1791 (1983).
62. Y. A. Vlasov and S. J. McNab, "Losses in single-mode silicon-on-insulator strip waveguides and bends," *Opt. Express* **12**, 1622–1631 (2004).
63. J. T. Kim, S. Park, J. J. Ju, S. Lee, and S. Kim, "Low bending loss characteristics of hybrid plasmonic waveguide for flexible optical interconnect," *Opt. Express* **18**, 24213–24220 (2010).

64. V. Astley, J. Scheiman, R. Mendis, and D. M. Mittleman, "Bending and coupling losses in terahertz wire waveguides," *Opt. Lett.* **35**, 553–555 (2010).
65. J. T. Lu, Y. C. Hsueh, Y. R. Huang, Y. J. Hwang, and C. K. Sun, "Bending loss of terahertz pipe waveguides," *Opt. Express* **18**, 26332–26338 (2010).
66. D. Marcuse, "Curvature loss formula for optical fibers," *J. Opt. Soc. Am.* **66**, 216–220 (1976).
67. R. T. Schermer and J. H. Cole, "Improved bend loss formula verified for optical fiber by simulation and experiment," *IEEE J. Quantum Electron.* **43**, 899–909 (2007).
68. K. Nallappan, H. Guerboukha, C. Nerguizian, and M. Skorobogatiy, "Live streaming of uncompressed 4K video using terahertz wireless links," in *IEEE International Conference on Communications (ICC)* (IEEE, 2018), pp. 1–7.
69. K. Nallappan, H. Guerboukha, C. Nerguizian, and M. Skorobogatiy, "Live streaming of uncompressed HD and 4K videos using terahertz wireless links," *IEEE Access* **6**, 58030–58042 (2018).
70. T. Nagatsuma and K. Kazutoshi, "Photonicly-assisted 300-GHz wireless link for real-time 100-Gbit/s transmission," in *IEEE MTT-S International Microwave Symposium (IMS)* (IEEE, 2014), pp. 1–4.
71. S. F. Zhou, L. Reekie, H. P. Chan, Y. T. Chow, P. S. Chung, and K. M. Luk, "Characterization and modeling of Bragg gratings written in polymer fiber for use as filters in the THz region," *Opt. Express* **20**, 9564–9571 (2012).
72. I. Yamada, K. Takano, M. Hangyo, M. Saito, and W. Watanabe, "Terahertz wire-grid polarizers with micrometer-pitch Al gratings," *Opt. Lett.* **34**, 274–276 (2009).
73. Y. M. Shin, L. R. Barnett, D. Gamzina, Jr., N. C. Luhmann, M. Field, and R. Borwick, "Terahertz vacuum electronic circuits fabricated by UV lithographic molding and deep reactive ion etching," *Appl. Phys. Lett.* **95**, 181505 (2009).
74. T. Rossner, R. Sarwar, A. Lyashenko, E. Dörsam, and R. Werthschützky, "B3. 4-hot stamped conductors on nano-micro wires made by electroplating for medical sensors and micro-implants," in *Proceedings Sensor* (2013), pp. 248–251.
75. H. Lee and P. A. Govind, "Add-drop multiplexers and interleavers with broad-band chromatic dispersion compensation based on purely phase-sampled fiber gratings," *IEEE Photon. Technol. Lett.* **16**, 635–637 (2004).
76. E. I. Simakov, C. E. Heath, D. Y. Shchegolkov, M. J. Kelly, and B. D. Schultz, "Fabrication and testing of channel-drop filters at millimeter waves," in *International Conference on Infrared, Millimeter, and Terahertz Waves* (IEEE, 2011), pp. 1–3.
77. E. I. Simakov, L. M. Earley, C. E. Heath, D. Y. Shchegolkov, and B. D. Schultz, "First experimental demonstration of a photonic band gap channel-drop filter at 240 GHz," *Rev. Sci. Instrum.* **81**, 104701 (2010).
78. M. Shalaby, M. Peccianti, Y. Ozturk, M. Clerici, I. Al-Naib, L. Razzari, T. Ozaki, A. Mazhorova, M. Skorobogatiy, and R. Morandotti, "Terahertz Faraday rotation in a magnetic liquid: high magneto-optical figure of merit and broadband operation in a ferrofluid," *Appl. Phys. Lett.* **100**, 241107 (2012).